PHYSICAL REVIEW FLUIDS **7**, 093302 (2022)

Hysteresis in viscoelastic flow instability of confined cylinders

Manish Kumar and Arezoo M. Ardekani
Department of Mechanical Engineering, Purdue University, West Lafayette, Indiana 47907, USA

(Received 11 March 2022; accepted 29 August 2022; published 29 September 2022)

Viscoelastic flow through porous media is relevant in many industrial and biological applications including enhanced oil recovery and biofluids' transport inside the body, where the presence of large polymeric stresses in the porous media leads to viscoelastic instability. In the present study, we numerically investigate viscoelastic instability-induced flow states in the channels consisting of (i) a single cylinder and (ii) two streamwise located cylinders. We unravel the presence of a hysteresis for pulsatile viscoelastic flows. For both geometries, the quantitative value of flow asymmetry around the cylinder resulting from the viscoelastic instability forms a closed hysteresis loop. We investigate the effects of fluid rheological properties and periodic inlet flow rates on the hysteresis loop.

DOI: 10.1103/PhysRevFluids.7.093302

I. INTRODUCTION

The flow of viscoelastic fluids through confined geometries is common in several biological, geophysical, and industrial processes such as targeted drug delivery, biofilm transport, and enhanced oil recovery [1–3]. The flow of mucus through ciliary epithelial surfaces and the transport of interstitial fluid through tissues are some of the examples of the flow of viscoelastic biological fluids through confined geometries [4]. The biopolymers secreted by the bacteria impart viscoelastic properties to biofilms, which flow through confined pores of rock and soil [5]. The transport of biofilm also occurs through the poroelastic tissues inside the body in the case of bacterial infection [2]. During enhanced oil recovery and groundwater remediation, polymeric solutions are injected into the porous rocks to mobilize capillary trapped nonaqueous liquids [3,6]. The microstructure of porous media contains curved surfaces [7,8]. The stretching of polymeric chains along the curvature as the viscoelastic solution passes through porous media creates large elastic stresses [9], which induces viscoelastic instability when the Weissenberg number is greater than a critical value [10,11]. The Weissenberg number (Wi) is a dimensionless parameter representing the ratio of elastic to viscous forces in viscoelastic flows [12]. Viscoelastic instabilities manifest into symmetry breaking [13,14], time-dependent flows [15], enhanced transport [16], elevated mixing [17], and abnormal rise of pressure drop [18] in viscoelastic flows depending on the geometry, elastic stress, and fluid rheology.

Simple isolated geometries such as cross-slot, isolated constriction, and confined cylinder have been used to infer some information about viscoelastic instabilities in the different portions of a porous geometry [1]. Elastic instability induces symmetry-breaking transition at a small Wi and time-dependent flow at a large Wi for viscoelastic flow through a cross-slot geometry [13,14,19]. The formation of unstable eddies takes place upstream of a sudden constriction [20,21] to mitigate the elastic stress induced due to the alignment of polymeric chains [22–25]. For viscoelastic flows around a confined cylinder, viscoelastic instability leads to the formation of eddies upstream of the cylinder at a large blockage ratio (>0.5) [26–28], whereas the flow becomes asymmetric around the cylinder for the geometries with a small blockage (<0.5). The manifestation of instability occurs downstream of the cylinder for the geometry with a small blockage [29,30]. The channels having

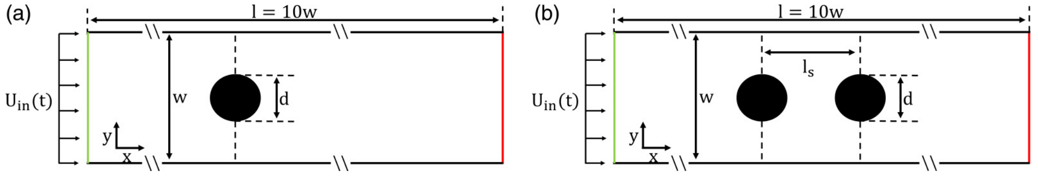

FIG. 1. Schematic of the geometries used for simulations: (a) a single cylinder located inside a channel and (b) a pair of streamwise located cylinders inside a channel. $U_{\text{in}}(t)$ represents time-dependent inlet flow velocity. Channel length, channel width, and cylinder diameter have been denoted by l, w, and d, respectively. The separation between cylinders for the channel consisting of a pair of cylinders is $l_s = 2d$. The values of different geometrical parameters are $l = 4$ mm, $w = 0.4$ mm, and $d = 160$ μm, respectively. The channel length is much larger than the width ($l = 10w$) and cylinder diameter ($l = 25d$) to avoid any entrance or exit effect (Appendix A 1). Black solid lines represent solid boundaries, whereas green and red lines indicate inlet and outlet, respectively.

an array of contractions and cylinders have been widely used as a one-dimensional (1D) model of porous geometry to investigate the viscoelastic interaction between the successive pores and obstacles [31–34]. Viscoelastic flows through channels consisting of multiple pores and cylinders lead to the formation of distinct steady and transient flow states due to viscoelastic instabilities [34–38]. The pore-scale viscoelastic instability ultimately regulates the sample-scale transport in 2D porous geometries [16,39,40]. Viscoelastic instability in a 3D porous geometry induces a chaotic flow due to complex connectivity and enhanced disorder, which leads to an abnormal rise of flow resistance [18].

The topology of the polymeric stress field regulates the formation of distinct pore-scale flow states in viscoelastic flows [36,38,41]. The magnitude of polymeric stress depends on the stretching of the polymeric chains and the stretching or relaxation of these chains occurs in finite time [9]. Therefore, viscoelastic instability-induced flow states exhibit hysteresis when the flow rate (or Wi) is time dependent. In the natural and industrial processes, the mass flow rate of viscoelastic fluids through confined geometries is often transient due to either time-dependent injection or viscoelastic instabilities. The time-dependent injection rate of displacing fluid suppresses viscous fingering instability [42–44]. Hence, it is desirable to inject displacing fluids into the reservoirs with a transient flow rate to enhance the oil recovery [45]. In natural processes such as ciliary motion-induced flow of mucus through cilia-covered epithelial surfaces, the flow rate is transient due to periodic beating of cilia [46,47]. Furthermore, even for a constant sample-scale flow rate of polymeric solution through porous media, the velocity fluctuations induced by viscoelastic instability lead to a locally transient flow rate of viscoelastic fluid in the microstructures of the porous media [18,40]. Therefore, it is essential to understand viscoelastic instability for transient flow rates through confined geometries. In the present work, we study pulsatile viscoelastic flows through channels consisting of cylinders and investigate hysteresis in the viscoelastic instability-induced flow states. Further, we investigate the effect of fluid's rheological parameters and the different parameters of transient flow on the hysteresis.

II. GEOMETRIES AND GOVERNING EQUATIONS

In the present work, we have numerically studied hysteresis in the viscoelastic instability-induced flow states in a channel having one or two cylinders (Fig. 1). The flow of incompressible viscoelastic fluid is described by the conservation of mass and momentum:

$$\nabla \cdot \mathbf{u} = 0, \tag{1}$$

$$\rho\left(\frac{\partial \mathbf{u}}{\partial t} + \mathbf{u} \cdot \nabla \mathbf{u}\right) = -\nabla p + \nabla \cdot \boldsymbol{\tau}, \tag{2}$$

where ρ is the fluid density, while $\mathbf{u}$ and p are the velocity and pressure fields, respectively. The variable $\boldsymbol{\tau}$ represents the stress tensor, which has two components coming from the solvent ($\boldsymbol{\tau_s}$) and the presence of polymeric chains ($\boldsymbol{\tau_p}$). For Newtonian solvents, $\boldsymbol{\tau_s}$ can be calculated as $\boldsymbol{\tau_s} = \eta_s(\nabla\mathbf{u} + \nabla\mathbf{u}^T)$, where η_s is the viscosity of the solvent. There are many mathematical models available to calculate the polymeric contribution of the stress tensor ($\boldsymbol{\tau_p}$) [48,49]. We choose the FENE-P constitutive model to calculate $\boldsymbol{\tau_p}$. The FENE-P model includes fluid elasticity and shear-thinning effects which are primary characteristics of most polymeric solutions and also considers the finite stretching of the polymeric chains [49,50]. The governing equation for $\boldsymbol{\tau_p}$ considering the FENE-P constitutive model can be written as:

$$\boldsymbol{\tau}_p + \frac{\lambda}{f}\overset{\nabla}{\boldsymbol{\tau}}_p = \frac{a\eta_p}{f}(\nabla\mathbf{u} + \nabla\mathbf{u}^T) - \frac{D}{Dt}\left(\frac{1}{f}\right)[\lambda\boldsymbol{\tau}_p + a\eta_p\boldsymbol{\delta}], \tag{3}$$

where λ is the relaxation time of polymeric chains and $\boldsymbol{\delta}$ is the identity tensor. The material derivative is shown as $\frac{D}{Dt} = \frac{\partial}{\partial t} + \mathbf{u}\cdot\nabla$. The polymer viscosity is $\eta_p = \eta_0 - \eta_s$, where η_0 is the total viscosity of the polymeric solution in the limit of zero-shear rate. The function f has the following form:

$$f(\boldsymbol{\tau_p}) = \frac{L^2 + \frac{\lambda}{a\eta_p}\mathrm{tr}(\boldsymbol{\tau_p})}{L^2 - 3}, \tag{4}$$

where L^2 represents the maximum stretching of the polymeric chains and $a = L^2/(L^2 - 3)$. The value of L^2 used in the literature lies in the range of $L^2 = 10\text{–}1000$ [50–52] and it is worth noting that the FENE-P model reduces into the Oldroyd-B constitutive model [53] at a large value of L^2 (i.e., $L^2 \to \infty$), which is an excellent model for constant viscosity highly elastic fluids (i.e., Boger fluid [54]). The term $\overset{\nabla}{\boldsymbol{\tau}}_p$ used in the FENE-P model [Eq. (3)] represents the upper convective time derivative of $\boldsymbol{\tau_p}$ which is given by:

$$\overset{\nabla}{\boldsymbol{\tau}}_p = \frac{D\boldsymbol{\tau}_p}{Dt} - \boldsymbol{\tau}_p\cdot\nabla\mathbf{u} - \nabla\mathbf{u}^T\cdot\boldsymbol{\tau}_p. \tag{5}$$

The numerical simulation using the form of the FENE-P model described in Eq. (3) is challenging at high Weissenberg numbers due to the exponential profile of stress tensor in the regions of high deformation rate [55]. The log-conformation approach is an alternative method to perform numerical simulation at a large Wi, where the equations are solved for the logarithm of conformation tensor ($\boldsymbol{\Theta}$) rather than $\boldsymbol{\tau_p}$ [56,57]. This method by default ensures the positive definiteness of the stress tensor, which is essential for numerical stability at high Weissenberg numbers. The following relation has been then used to calculate the polymeric stress tensor ($\boldsymbol{\tau_p}$) from the log-conformation tensor ($\boldsymbol{\Theta}$):

$$\boldsymbol{\tau}_p = \frac{\eta_p}{\lambda}(fe^{\boldsymbol{\Theta}} - a\boldsymbol{\delta}). \tag{6}$$

We perform 2D numerical simulations for viscoelastic flows through the geometries shown in Figs. 1(a) and 1(b). The numerical simulations have been performed using OpenFOAM, which is an open-source CFD framework based on the finite-volume method [58]. We integrate viscoelastic solver RheoTool [59] with OpenFOAM and use the log-conformation approach to calculate the polymeric stress tensor [59,60]. Gauss's theorem has been used to calculate the cell gradient (Gauss linear) and divergence [59]. The convective terms in the governing equations have been discretized using the Gaussian deferred correction component-wise schemes (GaussDefCmpw), where specifically the "CUBISTA" scheme has been used for the convective terms in the polymeric stress equation. The scheme based on the Gauss theorem has been also used to discretize the Laplacian terms since the Laplacian operator can be considered as a combination of the divergence and gradient operators. For the temporal evolution of the solution, we have used the Crank-Nicolson scheme.

We have used $n_x \times n_y = 2560 \times 256$ static grid points to discretize the computation domain, where the five layers in the vicinity of the cylinders have been further refined (Appendix A 2). n_x

TABLE I. The value of fluid and flow parameters used in the present study.

ρ	λ	U_{in}	β	L^2
1000 kg/m^3	1 s	0.05–0.5 mm/s	0.02–0.2	400–1000

and n_y are the grid points along the length and the width of the channel. The time-step size in the simulation has been controlled by the maximum Courant number (Co_{max}) and $\text{Co}_{\text{max}} = 0.025$ has been used throughout the study. The values of grid points and the maximum Courant number used for simulations are sufficient for the mesh and time-step-independent results (Appendix A 2). The inlet velocity in the channel is described by a uniform periodic triangular waveform [Fig. 3(a)]. The boundary conditions used at the inlet for polymeric stress tensor and pressure field are $\boldsymbol{\tau_p} = 0$ and $\mathbf{n} \cdot \nabla p = 0$, respectively. $\mathbf{n}$ is the unit vector normal to the surface. At the outlet, the boundary conditions used for velocity, polymeric stress tensor, and pressure are $\mathbf{n} \cdot \nabla u_i = 0$, $\mathbf{n} \cdot \nabla \tau_{p,ij} = 0$, and $p = 0$, respectively. u_i and $\tau_{p,ij}$ are the components of the velocity vector and polymeric stress tensor, respectively. No-slip and no-penetration boundary conditions have been used for the velocity field at the channel's walls and the cylinder's surface. Further, we use a linear extrapolation for polymeric stress tensor and zero gradient for the pressure field as the boundary conditions at the solid surfaces [59].

The Reynolds number (Re) is a relevant dimensionless number in any fluid flow, which represents the ratio of inertial to viscous forces and can be defined as $\text{Re} = \rho U_{\text{in}} d/\eta_0$. The effect of inertia is negligible as the Re is small ($\text{Re} = 0.0004-0.004$) due to the small length scale of the system. The Weissenberg number is defined as $\text{Wi} = \lambda U_{\text{in}}/d$ and its value lies in the range $\text{Wi} = 0-4$ in the present study. We vary U_{in} to change the Wi keeping other variables constant [Fig. 3(a)]. Therefore the elasticity number ($\text{El} = \text{Wi}/\text{Re} = \lambda\eta_0/\rho d^2$), which represents the ratio of elastic to inertial forces, has a constant value ($\text{El} = 781.25$) as it only depends on the fluid rheology and geometrical length scale. The elastic effects dominate the inertial effects since $\text{El} \gg 1$. We define viscosity-ratio $\beta = \eta_s/\eta_0$ to investigate the effect of shear-thinning behavior for the FENE-P constitutive model. The viscosity ratio and the relaxation time of the polymeric solutions generally used in the experiments are in the range of $\beta = 0.05-0.25$ [16,30] and $\lambda = 0.1-10$ s [13,16,30,40], respectively. The values of fluid properties and dimensional parameters used in the present study have been summarized in Table I. Throughout the study, we use λ to normalize time (t) and oscillation time period (T) and U_{in} to normalize velocity. The Deborah number, De, which measures the unsteadiness in viscoelastic flows [61], is directly related to the normalized oscillation time period as $\text{De} = 1/T$. The characteristic shear stress, $\eta_0 U_{\text{in}}/d$, has been used to the normalize the stress and pressure fields.

III. RESULTS AND DISCUSSION

A. A single cylinder located inside a channel

Viscoelastic flows through channels consisting of a single cylinder have been widely explored in the literature assuming constant mass flow rate [28–30]. However, despite the practical relevance, viscoelastic instability in the confined geometry having a transient mass flow rate has not been explored. For steady mass flow rate, viscoelastic instability induces flow asymmetry around the confined cylinder for the Wi greater than a critical value (Wi_{cr}) [30]. To identify the critical Wi required for the flow asymmetry in the present study, we first perform simulations considering constant flow rates [Fig. 2(a)]. To quantify the flow asymmetry around the cylinder, an asymmetry parameter (I) has been defined as:

$$I = \frac{|Q_{\text{upper}} - Q_{\text{lower}}|}{Q_{\text{upper}} + Q_{\text{lower}}}, \tag{7}$$

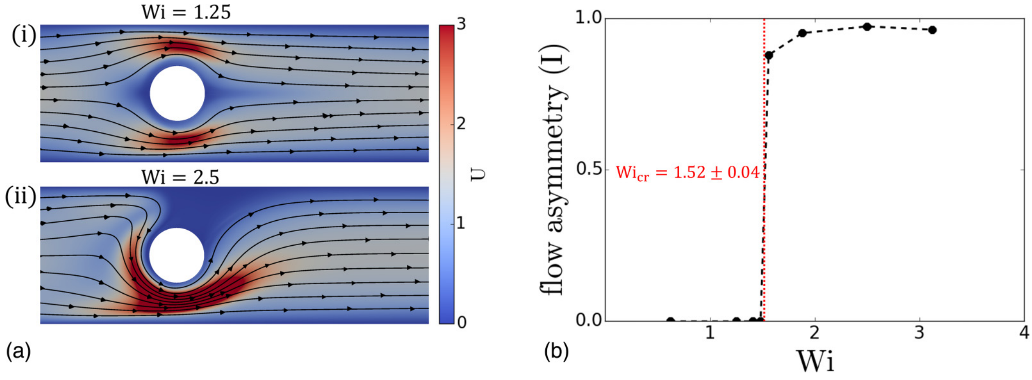

FIG. 2. (a) Velocity field for the viscoelastic flow around a confined cylinder at (i) $\mathrm{Wi} = 1.25$ and (ii) $\mathrm{Wi} = 2.5$. (b) Flow asymmetry, I, for the viscoelastic flow around a confined cylinder at different Wi. The symbol and the error bars represent the mean value and the standard deviation, respectively. The standard deviation is very small as the flow remains almost steady (Appendix A 3). The fluid rheological parameters are $\beta = 0.05$ and $L^2 = 1000$.

where Q_{upper} represents the mass flow rate through the gap between the cylinder and upper wall and Q_{lower} represents the mass flow rate through the gap between the cylinder and lower wall. The value of I varies from $I = 0$ for symmetric flow to $I = 1$ when the entire fluid passes through one of the gaps. $\mathrm{Wi}_{\mathrm{cr}}$ has been defined as the onset of the increase of I and its value for a fluid with $\beta = 0.05$ and $L^2 = 1000$ lies between $\mathrm{Wi} = 1.48$ and $\mathrm{Wi} = 1.56$ [Fig. 2(b)]. Therefore, we consider $\mathrm{Wi}_{\mathrm{cr}} = 1.52 \pm 0.04$.

To investigate the effect of transient flow rate on the viscoelastic instability-induced flow, we consider a time-dependent inlet velocity, corresponding to a transient Wi as shown in Fig. 3(a). In this study, we change minimum Wi ($\mathrm{Wi}_{\mathrm{min}}$), maximum Wi ($\mathrm{Wi}_{\mathrm{max}}$), and time period (T) of the oscillatory Wi. Figure 3(b) depicts the value of flow asymmetry (I) for the multiple oscillations of Wi at a fixed oscillation's time period ($T = 10$). The value of I converges to a closed loop after a few initial oscillations of Wi. The closed loop of the flow asymmetry leads to two possible values of I at a given Wi, depending on the route that has been followed to get the specific value of Wi [Fig. 3(b)]. Thus, the flow asymmetry exhibits hysteresis for oscillatory flow rates. At large Wi, the flow asymmetry saturates as the entire fluid passes through either of the gaps. Therefore, two different branches of the hysteresis loop coincide with each other [Fig. 3(b)]. However, we do not see the saturation of flow asymmetry at the lower limit of Wi. The value of Wi linearly varies forth and back from $\mathrm{Wi}_{\mathrm{min}} < \mathrm{Wi}_{\mathrm{cr}}$ to $\mathrm{Wi}_{\mathrm{max}} > \mathrm{Wi}_{\mathrm{cr}}$ [Fig. 3(a)]. However, the flow around the cylinder always remains asymmetric (i.e., $I > 0$) after achieving the hysteresis loop [Fig. 3(b)] and we do not see the transition from asymmetric to symmetric flow state as Wi becomes less than $\mathrm{Wi}_{\mathrm{cr}}$. The size and shape of the hysteresis loop significantly depend on the rate of change of Wi [Figs. 3(c) and 3(d)]. The area of the loop increases as the time period increases and the hysteresis loop changes from a triangular shape at $T = 10$ to an elliptical shape at $T = 20$ to a squarelike shape at $T = 40$.

To understand the origin of hysteresis and the flow state at the different branches of the hysteresis loop, we plot the flow field and stress field at a fixed $\mathrm{Wi}(<\mathrm{Wi}_{\mathrm{cr}})$ but for the different branches of the hysteresis loop at $T = 20$ [Fig. 3(c)] in Fig. 4. Streaks of large polymer stress induce flow separation and lead to the formation of distinct flow states [36,38]. The viscoelastic flow around a cylinder creates a long elastic wake [30,62]. At $\mathrm{Wi} > \mathrm{Wi}_{\mathrm{cr}}$, the elastic wake downstream of the cylinder becomes asymmetric, leading to an asymmetric flow state [30]. The flow states shown in Fig. 4 correspond to different branches of the hysteresis loop. Therefore, despite having the same Wi, they have different stress field depending on the route [Figs. 4(d), 4(e), and 4(f)]. The location shown by (●) in Fig. 3(c) belongs to the branch corresponding to the first oscillation of Wi and

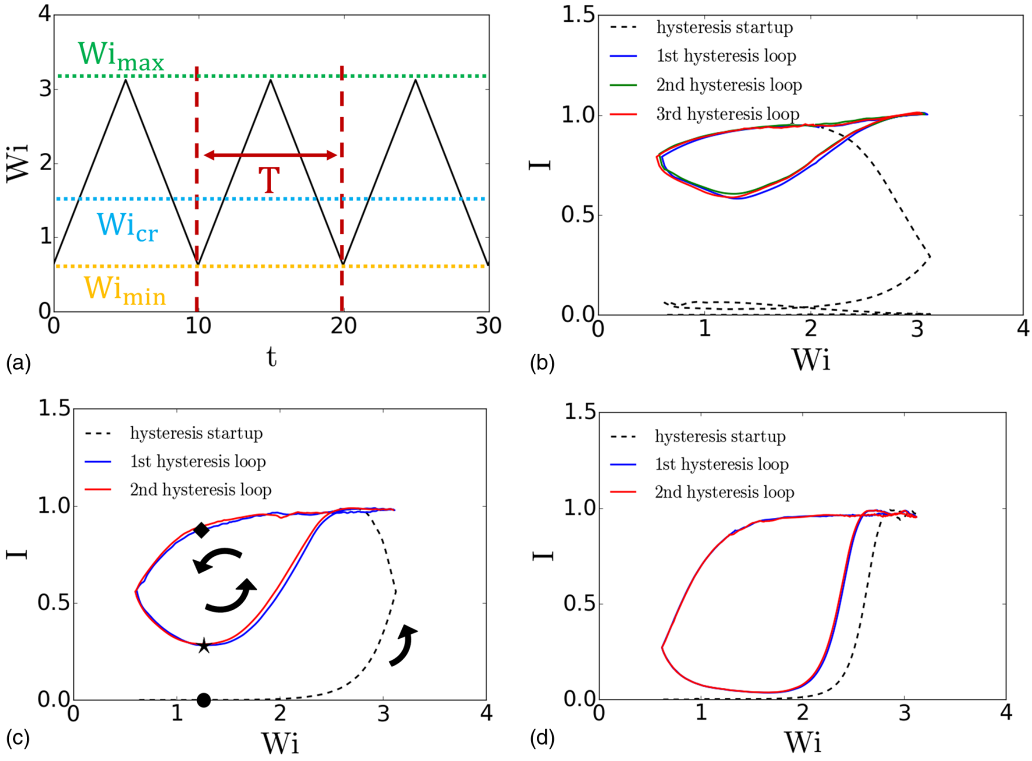

FIG. 3. (a) The profile of time-dependent oscillatory Wi used in the simulation. $\mathrm{Wi_{min}}$, $\mathrm{Wi_{max}}$, and T are the minimum value, maximum value and time period of Wi. The value of flow asymmetry at different Wi for (b) $T = 10$, (c) $T = 20$, and (d) $T = 40$. Black dashed lines show the startup regime for the hysteresis, whereas solid lines represent different hysteresis loops. The values of other parameters are $\beta = 0.05$, $L^2 = 1000$, $\mathrm{Wi_{min}} = 0.62$, and $\mathrm{Wi_{max}} = 3.12$.

$\mathrm{Wi} < \mathrm{Wi_{cr}}$. Therefore, the stress topology is symmetric [Fig. 4(d)], leading to a symmetric flow state at this location [Fig. 4(a)]. The location indicated by (♦) in Fig. 3(c) is on the branch of the hysteresis loop corresponding to the decreasing value of Wi after attaining $\mathrm{Wi_{max}}$ and it has an asymmetric flow state despite $\mathrm{Wi} < \mathrm{Wi_{cr}}$ [Fig. 4(b)]. The topology of stress field as well as the flow state at $\mathrm{Wi_{max}}$ is asymmetric as $\mathrm{Wi_{max}} > \mathrm{Wi_{cr}}$ and the location denoted by (♦) is in the route decreasing from $\mathrm{Wi_{max}}$ to $\mathrm{Wi_{min}}$. The topology of the stress field has a memory and it requires a finite time to transform itself. Therefore, the polymeric stress topology at the location denoted by (♦) remains asymmetric despite $\mathrm{Wi} < \mathrm{Wi_{cr}}$ [Fig. 4(e)] and induces an asymmetric flow state [Fig. 4(b)]. In fact, the topology of stress field is not able to completely transform from an asymmetric profile at $\mathrm{Wi_{max}}$ to a perfectly symmetric profile at $\mathrm{Wi_{min}}$. Therefore it has $I > 0$ even at $\mathrm{Wi_{min}}$ in the hysteresis loop. However, the value of I at $\mathrm{Wi_{min}}$ is smaller than that at $\mathrm{Wi_{max}}$ indicating that the flow state is less asymmetric at $\mathrm{Wi_{min}}$ than $\mathrm{Wi_{max}}$ [Fig. 3(c)]. The point indicated by (★) on the hysteresis loop [Fig. 3(c)] is on the branch where Wi increases from $\mathrm{Wi_{min}}$ to $\mathrm{Wi_{max}}$. Along this branch, first, the stress topology continues to transform toward a symmetric topology [Fig. 4(f)], which leads to the decrease in I as Wi increases. Therefore, at the location denoted by (★) on the hysteresis loop, the flow state is less asymmetric [Fig. 4(c)] than the flow state at the location indicated by (♦) on the loop (Fig. 4(b)]. After achieving a minimum value of $I (> 0)$, the stress topology again starts to transform toward a more asymmetric topology as Wi further increases, which leads to the increase in I with Wi [Fig. 3(c)]. Thus, the stress topology and flow state do not become symmetric after attaining the hysteresis loop. For the quasistatic variation of flow rate (or

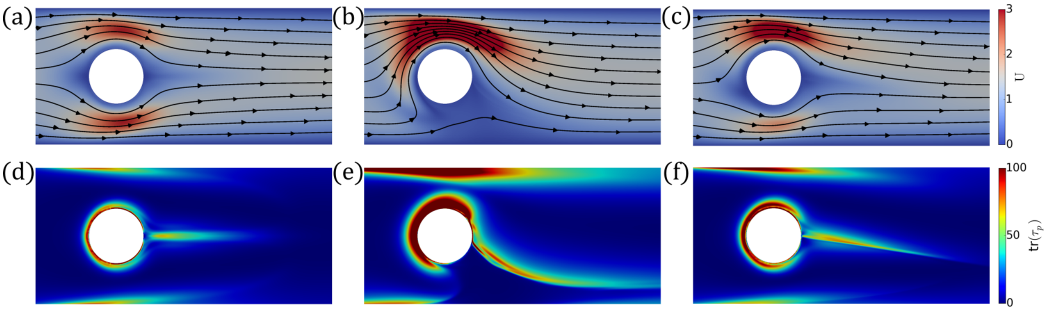

FIG. 4. [(a)–(c)] Flow field and [(d)–(f)] the trace of polymeric stress field at $\mathrm{Wi} = 1.25(< \mathrm{Wi}_{cr})$ for the different branches of the hysteresis loop shown in Fig. 3(c). The flow states shown in [(a) and (d)], [(b) and (e)], and [(c) and (f)] correspond to the locations indicated by filled circle (●), filled diamond (◆), and filled star (★) in Fig. 3(c), respectively. Other parameters are $\beta = 0.05$, $L^2 = 1000$, $T = 20$, $\mathrm{Wi}_{\mathrm{min}} = 0.62$, and $\mathrm{Wi}_{\mathrm{max}} = 3.12$.

Wi) considered in the previous experiments [29,63], the polymeric stress had sufficient time to relax after each stepwise increment/decrement of Wi (Appendix A 4). Therefore, the hysteresis was not reported in the previous experiments performed using a quasistatic variation of the flow rate [29,63].

Further, we investigate the effect of time period, minimum Wi, and maximum Wi on the hysteresis, and quantify the area of the hysteresis loop (A_{loop}) and the minimum value of the asymmetry parameter (I_{min}) in the hysteresis loop. A_{loop} physically represents the strength of the hysteresis and I_{min} determines the deviation of the hysteresis loop from the symmetric flow state. A_{loop} increases as the time period (T) of the oscillation of Wi increases, whereas I_{min} decreases with the increasing value of T [Fig. 5(a)]. The flow rate (i.e., Wi) changes slowly as the time period of the oscillation increases, providing a longer time for the stress field to transform from asymmetric to the symmetric topology. Therefore, the value of I_{min} decreases as T increases [Fig. 3(d)]. The size of the hysteresis loop increases as the value of I_{min} decreases. Hence, the area of the hysteresis loop increases with T [Fig. 5(a)]. The range of Wi increases as the lower limit of Wi decreases and the value of I does not saturate at $\mathrm{Wi}_{\mathrm{min}}$ [Fig. 3(c)]. Therefore, I_{min} decreases as the lower limit of Wi decreases (Fig. 5(b)], which also delays the saturation of I to a larger value of Wi. The combined effect of the increase of Wi range, decrease of I_{min}, and delaying the saturation of flow asymmetry leads to the increase of A_{loop} as $\mathrm{Wi}_{\mathrm{min}}$ decreases [Fig. 5(b)]. The range of Wi also increases with the increasing value of upper limit of Wi. However, the value of I_{min} increases [Fig. 5(c)] and the flow asymmetry saturates at a smaller Wi as $\mathrm{Wi}_{\mathrm{max}}$ increases. Therefore, despite the increase of the range of Wi, the area of the hysteresis loop decreases as the value of $\mathrm{Wi}_{\mathrm{max}}$ increases [Fig. 5(c)].

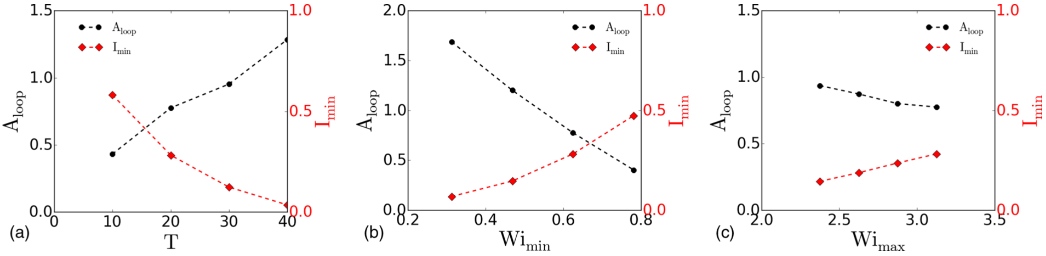

FIG. 5. The area of hysteresis loop (A_{loop}) and the minimum value of flow asymmetry in the hysteresis loop (I_{min}) for different values of (a) oscillation time period (T), (b) minimum Wi ($\mathrm{Wi}_{\mathrm{min}}$), and (c) maximum Wi ($\mathrm{Wi}_{\mathrm{max}}$). The values of other parameters are $\mathrm{Wi}_{\mathrm{min}} = 0.62$ and $\mathrm{Wi}_{\mathrm{max}} = 3.12$ for (a), $T = 20$ and $\mathrm{Wi}_{\mathrm{max}} = 3.12$ for (b), and $\mathrm{Wi}_{\mathrm{min}} = 0.62$ and $T = 20$ for (c). The rheological parameters are $\beta = 0.05$ and $L^2 = 1000$.

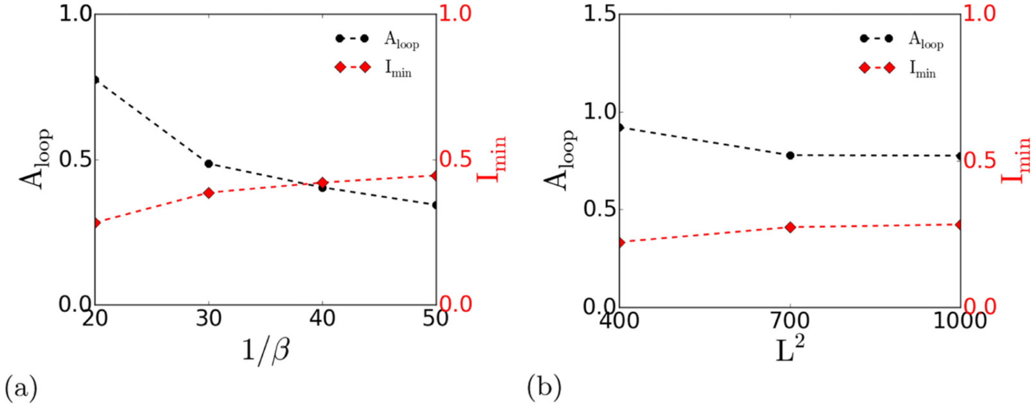

FIG. 6. The area of hysteresis loop (A_{loop}) and the minimum value of flow asymmetry in the hysteresis loop (I_{min}) for different values of (a) viscosity ratio (β) at $L^2 = 1000$ and (b) polymeric chains' extensibility (L^2) at $\beta = 0.05$. Other parameters are $T = 20$, $\mathrm{Wi}_{\mathrm{min}} = 0.62$, and $\mathrm{Wi}_{\mathrm{max}} = 3.12$.

We also explore the effect of fluid rheological parameters on the hysteresis. The value of $\mathrm{Wi}_{\mathrm{cr}}$ required for the flow asymmetry decreases with the increasing strength of shear-thinning [29,30]. Therefore, the value of I in the hysteresis loop saturates at a lower Wi and the range of Wi wherein I has two distinct values decreases as β decreases. This leads to the enhancement of I_{min} and the decline of A_{loop} as the value β decreases [Fig. 6(a)]. For a weakly shear-thinning fluid (i.e., $1/\beta = 10$), the flow around the cylinder remains symmetric for the range of Wi considered in the present study, and hence the formation of the hysteresis loop does not take place. The elastic property of fluid increases as the extensibility of the polymeric chains (L^2) increases and a stronger elastic fluid has a smaller $\mathrm{Wi}_{\mathrm{cr}}$ for the instability [30]. Therefore, the flow asymmetry saturates at a smaller Wi as L^2 increases and leads to the increase of I_{min} and the decrease of A_{loop} as the elasticity of fluid increases [Fig. 6(b)].

B. Two cylinders located inside a channel

In the channel consisting of two streamwise located cylinders [Fig. 1(b)], viscoelastic instability induces three distinct flow states in the region between the cylinders [36]. The transitions between these distinct flow states are characterized by two critical Wi ($\mathrm{Wi}_{\mathrm{cr1}}$ and $\mathrm{Wi}_{\mathrm{cr2}}$). The flow is symmetric and eddy free for $\mathrm{Wi} < \mathrm{Wi}_{\mathrm{cr1}}$ (flow type-1). After the first transition ($\mathrm{Wi}_{\mathrm{cr1}} < \mathrm{Wi} < \mathrm{Wi}_{\mathrm{cr2}}$), a pair of recirculating eddies appear in the region between the cylinders (type-2). Whereas, the eddies disappear and the flow around cylinders becomes asymmetric for $\mathrm{Wi} > \mathrm{Wi}_{\mathrm{cr1}}$ (type-3). To investigate the hysteresis in viscoelastic instability-induced flow states between two cylinders, we consider the range of time-dependent Wi such that $\mathrm{Wi}_{\mathrm{min}} < \mathrm{Wi}_{\mathrm{cr1}} < \mathrm{Wi}_{\mathrm{cr2}} < \mathrm{Wi}_{\mathrm{max}}$. Figure 7(a) depicts the flow asymmetry (I) around the front cylinder for the multiple oscillations of Wi at $T = 40$. The route of I during the increase of Wi from $\mathrm{Wi}_{\mathrm{min}}$ to $\mathrm{Wi}_{\mathrm{max}}$ is different than the route observed when Wi decreases from $\mathrm{Wi}_{\mathrm{max}}$ to $\mathrm{Wi}_{\mathrm{min}}$ [Fig. 7(a)]. However, the value of I makes a closed loop during the complete oscillation of Wi, indicating the hysteresis in the flow states. The flow around the cylinder remains symmetric ($I = 0$) even after the first transition ($\mathrm{Wi}_{\mathrm{cr1}} < \mathrm{Wi} < \mathrm{Wi}_{\mathrm{cr2}}$), wherein the eddies appear in the region between the cylinders (type-2) [36]. Therefore, we quantify the area occupied by the eddies (A_{eddy}) in the region between the cylinders to differentiate the flow state consisting of eddies (type-2) from the eddy-free symmetric (type-1) flow state [Fig. 7(b)]. A_{eddy} increases continuously due to a continuous change in Wi. We set $A_{\mathrm{eddy}} = 0.04$ as a critical value of A_{eddy} to identify the eddy-free symmetric (type-1) flow state, because A_{eddy} increases rapidly after $A_{\mathrm{eddy}} = 0.04$ [Fig. 7(b)]. The value of A_{eddy} also makes a closed loop and exhibits hysteresis. The portions of the hysteresis loop corresponding to the eddy free symmetric (type-1) and asymmetric

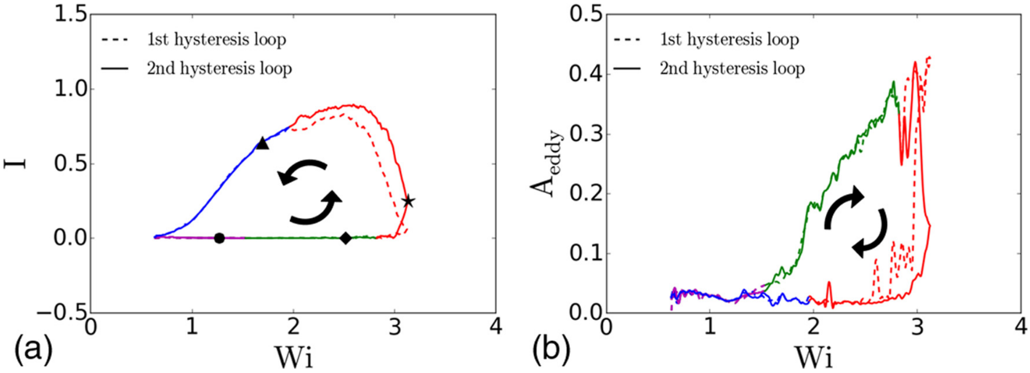

FIG. 7. (a) Flow asymmetry (I) around the front cylinder in the geometry having two streamwise located cylinders in a channel at $T = 40$. (b) The area occupied by eddies (A_{eddy}) in the region between the cylinders at $T = 40$. A_{eddy} has been normalized with $l_s d$. The portions of the hysteresis loop corresponding to the eddy free symmetric (type-1) and asymmetric (type-3) flow states have been indicated by magenta and blue colors, respectively. The green and red portions of the loop represent symmetric and asymmetric flow states with eddies between the cylinders, respectively. The values of other parameters are $\beta = 0.05$, $L^2 = 1000$, $\text{Wi}_{\text{min}} = 0.62$, and $\text{Wi}_{\text{max}} = 3.12$.

(type-3) flow states have been indicated by magenta and blue colors, respectively [Figs. 7(a) and 7(b)]. The hysteresis loops corresponding to the different oscillations of Wi collapse on each other except the portion indicated with the red color. The red portion of the loop represents an asymmetric flow state with eddies between the cylinders. This is an intermediate state between the flow state with eddies (type-2) and the eddy-free asymmetric flow state (type-3) [36]. Both A_{eddy} and I fluctuate for this flow state. Therefore, the values of A_{eddy} or I corresponding to the different oscillations of Wi do not perfectly collapse on each other [Figs. 7(a) and 7(b)]. Here onward, we refer to the symmetric and asymmetric flow states with eddies as type-2a (green color in the hysteresis loop) and type-2b (red color) flow state, respectively.

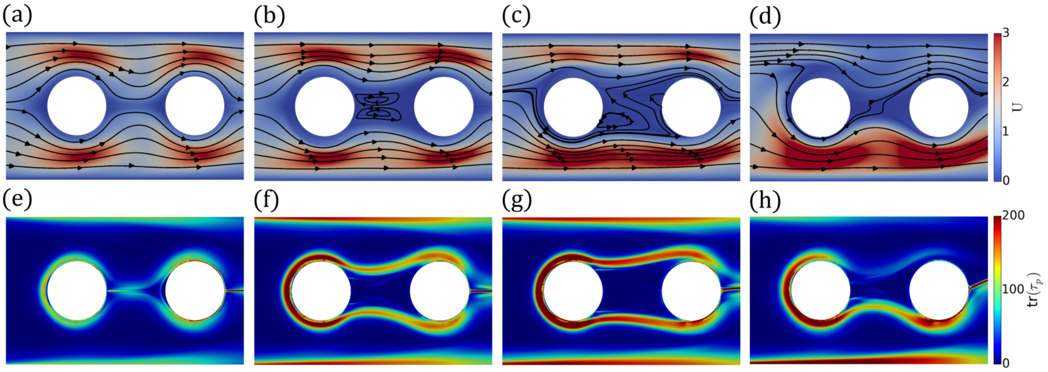

FIG. 8. [(a)–(d)] Flow field and [(e)–(h)] the trace of polymeric stress field corresponding to the different portions of the hysteresis loop shown in Fig. 7(a). The flow states shown in [(a) and (e)], [(b) and (f)], [(c) and (g)], and [(d) and (h)] correspond to the locations indicated by filled circle (●), filled diamond (♦), filled star (★), and filled triangle (▲) in Fig. 7(a) and represent flow states type-1, type-2a, type-2b, and type-3, respectively. The values of other parameters are $\beta = 0.05$, $L^2 = 1000$, $T = 40$, $\text{Wi}_{\text{min}} = 0.62$, and $\text{Wi}_{\text{max}} = 3.12$.

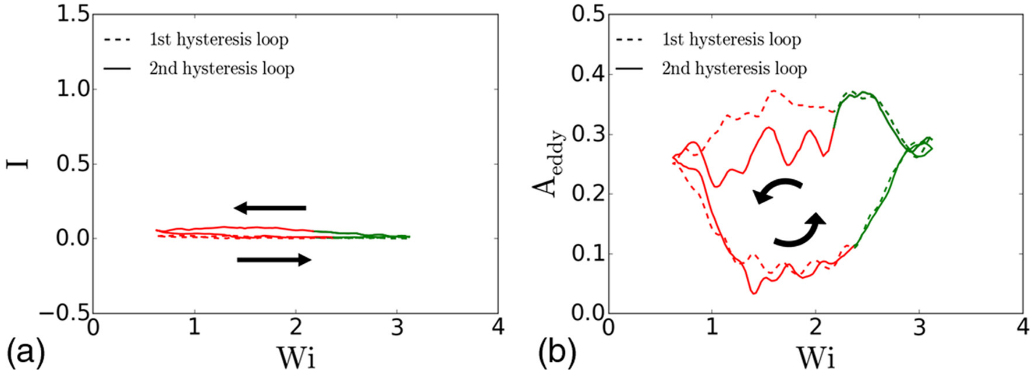

FIG. 9. (a) Flow asymmetry (I) around the front cylinder in the geometry consisting of two streamwise located cylinders at $T = 10$. (b) The area occupied by eddies (A_{eddy}) in the region between the cylinders at $T = 10$. A_{eddy} has been normalized with $l_s d$. The values of other parameters are $\beta = 0.05$, $L^2 = 1000$, $\text{Wi}_{\min} = 0.62$, and $\text{Wi}_{\max} = 3.12$.

The flow state representing each portion of the hysteresis loop has been shown in Fig. 8. These flow states correspond to the location indicated by different symbols on the hysteresis loop in Fig. 7(a). At the location indicated by (●) and (♦) in Fig. 7(a), the stress topology is symmetric [Figs. 8(e) and 8(f)], which induces symmetric flow states ($I = 0$) as shown in Figs. 8(a) and 8(b). The elastic wake in between the cylinders bifurcates in two symmetric branches after the first transition and encircles the region between the cylinders [Fig. 8(f)], leading to the formation of eddies between the cylinders [Fig. 8(b)]. The elastic wake has two branches even at the location indicated by (★) in the hysteresis loop [Fig. 8(g)]. However, the top branch starts to deviate from the rear cylinder [Fig. 8(g)] and hence the stress topology loses the symmetry. This leads to asymmetric flow around the cylinders ($I > 0$) and A_{eddy} becomes smaller [Fig. 8(c)]. Ultimately, the top branch of elastic wake completely disappears [Fig. 8(h)] for the location indicated by (▲) in Fig. 7(a). This topology of the stress field induces an eddy-free asymmetric flow state [Fig. 8(d)]. The stress field transforms from asymmetric to symmetric topology as Wi decreases from $\text{Wi}_{\max}$ to $\text{Wi}_{\min}$. Therefore, the symmetric flow states (flow type-1 and type-2a) do not appear and flow around the cylinders remains asymmetric ($I > 0$) in the route where Wi decreases from $\text{Wi}_{\max}$ to $\text{Wi}_{\min}$ [Fig. 7(a)].

A smaller time period (T) of the oscillation of Wi does not provide sufficient time for the transformation of the topology of the stress field. Therefore, it exhibits a fewer number of flow states during the complete oscillation of Wi. For a small time period ($T = 10$), the hysteresis loops of flow asymmetry (I) and eddies' area (A_{eddy}) have been shown in Fig. 9(a) and Fig. 9(b), respectively. After achieving the hysteresis loop, eddies exist in the region between the cylinders throughout the oscillation period [Fig. 9(b)]. In the portion of the hysteresis loop indicated by red color, the area occupied by eddies fluctuates [Fig. 9(b)], and flow around the cylinder becomes slightly asymmetric [Fig. 9(a)]. However, the eddy never disappears, and flow around the cylinder never becomes completely asymmetric at $T = 10$. Thus, unlike $T = 40$, the hysteresis at $T = 10$ exhibits only the flow states which have eddies (flow states type-2a and type-2b) and the transition happens between type-2a and type-2b flow states in the hysteresis loop [Fig. 9(b)].

To investigate the effect of the upper and lower limit of Wi on the hysteresis, we plot the flow asymmetry around the front cylinder [Figs. 10(a), 10(b) and 10(c)] and the area occupied by eddies [Figs. 10(d), 10(e) and 10(f)] at $T = 20$ for different values of $\text{Wi}_{\min}$ and $\text{Wi}_{\max}$. Unlike the hysteresis loop at $T = 10$, there is sufficient time available at $T = 20$ for the existence of eddy free symmetric (type-1) flow state. However, the time is not enough for the formation of eddy free asymmetric (type-3) flow state like the hysteresis loop at $T = 40$. Therefore, the hysteresis loop at $T = 20$ exhibits only two flow states [Figs. 10(a) and 10(d)]: eddy free symmetric flow state (flow

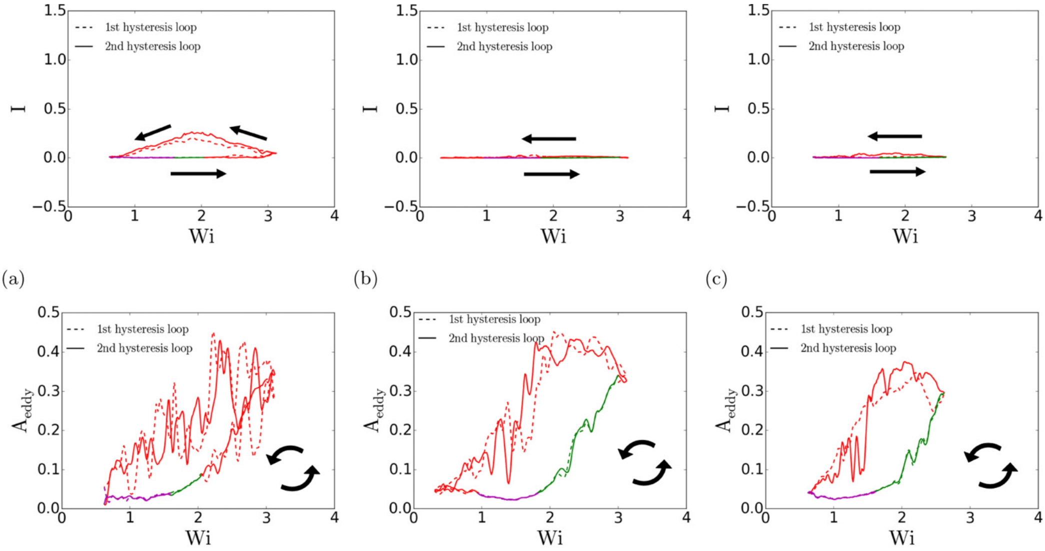

(a) (b) (c)

(d) (e) (f)

FIG. 10. [(a)–(c)] Flow asymmetry (I) around the front cylinder and [(d)–(f)] the area occupied by eddies (A_{eddy}) in the region between the cylinders for [(a) and (d)] $\mathrm{Wi}_{\mathrm{min}} = 0.62$, $\mathrm{Wi}_{\mathrm{max}} = 3.12$; [(b) and (e)] $\mathrm{Wi}_{\mathrm{min}} = 0.31$, $\mathrm{Wi}_{\mathrm{max}} = 3.12$; and [(c) and (f)] $\mathrm{Wi}_{\mathrm{min}} = 0.62$, $\mathrm{Wi}_{\mathrm{max}} = 2.62$. The values of other parameters are $\beta = 0.05$, $L^2 = 1000$, and $T = 20$. A_{eddy} has been normalized with $l_s d$.

state type-1) and flow state with eddies (type-2a and -2b). For ($\mathrm{Wi}_{\mathrm{min}} = 0.62$, $\mathrm{Wi}_{\mathrm{max}} = 3.12$), the asymmetric flow state containing eddies (type-2b) exists for a much longer time compared to the symmetric flow state with eddies (type-2a) [Fig. 10(d)], and the fluctuation of A_{eddy} leads to $I \neq 0$ [Fig. 10(a)]. As the value of $\mathrm{Wi}_{\mathrm{min}}$ decreases, the type-2a flow state exists for a longer time and the fluctuation of A_{eddy} for the type-2b flow state reduces [Fig. 10(e)], leading to an almost symmetric flow around the cylinder ($I \approx 0$) throughout the oscillation period [Fig. 10(b)]. The reduction of the value of $\mathrm{Wi}_{\mathrm{max}}$ has an effect similar to the reduction of $\mathrm{Wi}_{\mathrm{min}}$ [Figs. 10(c) and 10(f)]. The flow state type-2a exists for a longer time and the fluctuation of A_{eddy} also decreases as the value of $\mathrm{Wi}_{\mathrm{max}}$ reduces [Fig. 10(f)].

Fluid rheology also influences the hysteresis loop of I [Figs. 11(a) and 11(b)] and A_{eddy} [Figs. 11(c) and 11(d)]. The stability of the symmetric flow state increases as either the strength of shear-thinning decreases (i.e., β increases) or the elasticity of fluid decreases (i.e., L^2 decreases) [36]. Therefore, the symmetric flow state type-2a exists for a longer time at $\beta = 0.2$ [Fig. 11(c)] than $\beta = 0.05$ [Fig. 10(d)] and at $L^2 = 400$ [Fig. 11(d)] than $L^2 = 1000$ [Fig. 10(d)]. There also occurs a transition from type-2b to type-2a flow state at $\beta = 0.2$ [Fig. 11(c)], unlike the other scenarios at $T = 20$ where the transition happens directly from type-2b to type-1 flow state in the hysteresis loop. Therefore, the type-2a flow state exists in two different portions of the hysteresis loop at $\beta = 0.2$ [Fig. 11(c)]. The fluctuation of A_{eddy} reduces as β increases or L^2 decreases. Therefore, the value of I is smaller at $\beta = 0.2$ [Fig. 11(a)] and $L^2 = 400$ [Fig. 11(b)] than the value at $\beta = 0.05$ and $L^2 = 1000$ [Fig. 10(a)].

IV. CONCLUSIONS

Viscoelastic instabilities induce distinct flow states in different geometries, where the formation of the specific topology of the polymeric stress field regulates these flow states. Viscoelastic

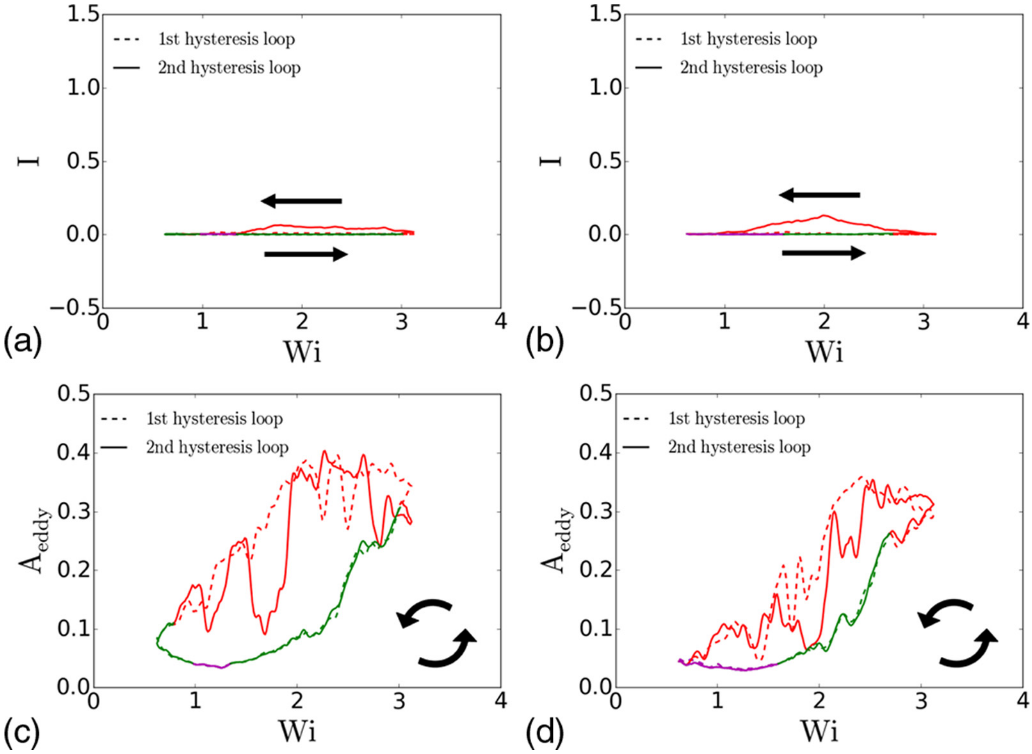

FIG. 11. [(a) and (b)] Flow asymmetry (I) around the front cylinder and [(c) and (d)] the area occupied by eddies (A_{eddy}) in the region between the cylinders for [(a) and (c)] $\beta = 0.2$ and $L^2 = 1000$ and [(b) and (d)] $\beta = 0.05$ and $L^2 = 400$. The values of other parameters are $\mathrm{Wi}_{\mathrm{min}} = 0.62$, $\mathrm{Wi}_{\mathrm{max}} = 3.12$, and $T = 20$. A_{eddy} has been normalized with $l_s d$.

instability-induced flow states exhibit hysteresis due to fluid memory. The volumetric flow rate of viscoelastic fluids through confined geometries is often transient in natural and industrial processes, like the cilia-induced flow of biological fluids and enhanced oil recovery. We investigate the hysteresis in the viscoelastic flow instability in the channels consisting of (i) a single cylinder and (ii) two streamwise located cylinders. For constant flow rates through the channel, the flow around the cylinder becomes asymmetric at $\mathrm{Wi} > \mathrm{Wi}_{\mathrm{cr}}$ in the geometry consisting of a single cylinder. However, for a pulsatile flow, the viscoelastic flow around the cylinder remains asymmetric even at $\mathrm{Wi} < \mathrm{Wi}_{\mathrm{cr}}$ and the flow asymmetry parameter undergoes a closed hysteresis loop. The hysteresis loop area increases with the time period of the pulsatile flow and decreases with the increasing value of the lower or upper limit of the flow rate. The loop area also decreases as the strength of shear-thinning or the extensibility of the polymeric chains increases. In the channel consisting of two streamwise located cylinders, the viscoelastic instability induces three distinct flow states, which are characterized by the flow asymmetry around the cylinders and the existence of eddies between the cylinders. Both the flow asymmetry and the area occupied by eddies form hysteresis loops for periodically varying flow rates. The number of distinct flow states obtained during the hysteresis varies from one to three depending on the time period of the oscillation. The symmetric flow states exist for a longer time during the periodic oscillation as the shear-thinning strength or the elasticity of the fluid decreases.

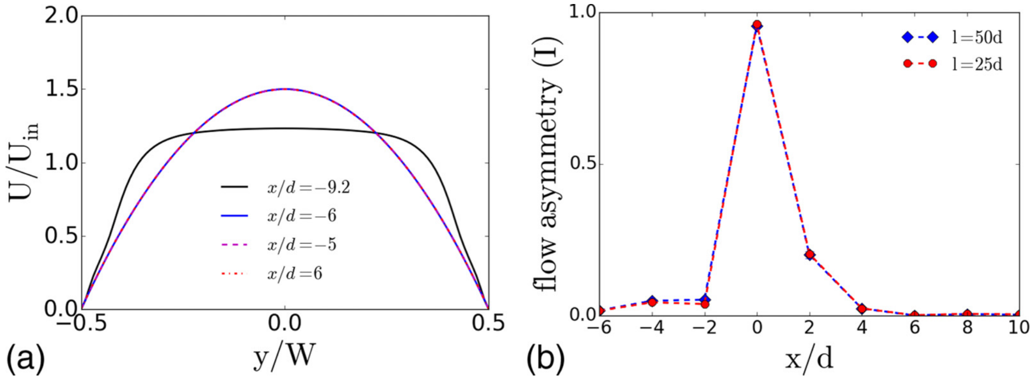

FIG. 12. (a) The velocity profile at different locations along the length of the channel ($l = 25d$) at Wi = 0.62 for the channel having a single cylinder. (b) Flow asymmetry (I) at different locations along the length of channel at Wi = 3.12 for the channels having length $l = 25d$ and $l = 50d$. The cylinder (the front cylinder in the channel having two cylinders) is located at $x = 0$. The entrance and the exit of the channel are at $x = -9.4d$ and $x = 15.6d$ for $l = 25d$, and $x = -21.9d$ and $x = 28.1d$ for $l = 50d$.

ACKNOWLEDGMENTS

A.M.A. acknowledges financial support from the National Science Foundation (NSF) through Grants No. CBET-1700961 and CBET-2141404.

APPENDIX

1. Effect of channel length on the instability

For a Newtonian flow through a channel, the hydrodynamic entrance length can be estimated as [64]:

$$L_{\text{entrance}} = 0.05\text{Re}_D D, \tag{A1}$$

where D and $\text{Re}_D = \rho U_{\text{in}} D/\mu$ are the hydraulic diameter of the channel and the Reynolds number based on the hydraulic diameter, respectively. For a Newtonian fluid, the hydrodynamic entrance length for the flow rate considered in the present study lies in the range of $L_{\text{entrance}} = 10^{-4}d - 5 \times 10^{-4}d$, where d is the cylinder diameter. The length of the channel in the present study is $25d$ and the cylinder (the front cylinder for the channel having two cylinders) is located $9.4d$ downstream from the inlet, which is much larger than the hydrodynamic entrance length. For a viscoelastic channel flow, the hydrodynamic entrance length can be larger than a Newtonian flow. Therefore, we have shown the velocity profile at different locations along the length of the channel in Fig. 12(a) for a viscoelastic flow. The velocity profile inside the channel becomes fully developed sufficiently upstream of the cylinder [Fig. 12(a)]. The exit effect is also negligible as the velocity downstream of the cylinder becomes fully developed much before the exit [Fig. 12(a)]. Further, to check the effect of the channel's length on the instability, we have plotted flow asymmetry (I) at the locations close to the cylinder at the maximum Wi considered in the present study (Wi = 3.12) for the channels having lengths $l = 25d$ and $l = 50d$ [Fig. 12(b)]. There is not any significant effect of the enhancement of the channel length on the instability even at the maximum Wi [Fig. 12(b)]. In fact, the effect of the cylinder vanishes for $x/d > 6$ and the flow inside the channel again becomes symmetric ($I = 0$) [Fig. 12(b)]. Thus, the flow and polymeric stress equilibrate much before the exit even at the maximum Wi. Taken together, these results show that the entrance and exit effects are not present in the present study.

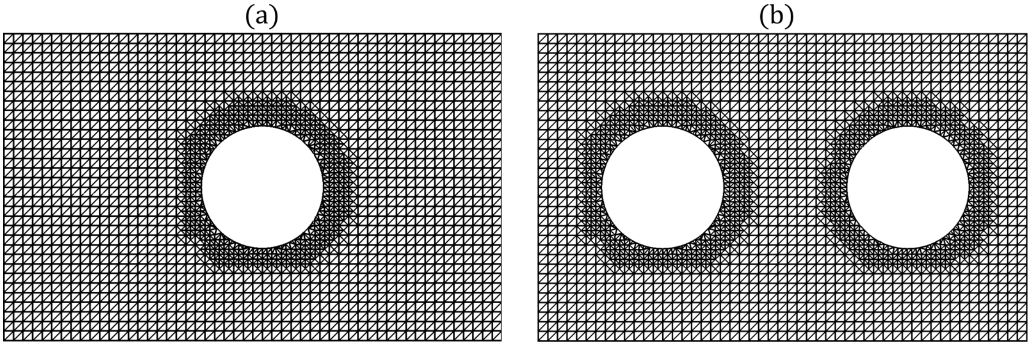

FIG. 13. Cartoons showing coarse numerical meshes (320 × 32) close to the cylinders for the channels having (a) a single cylinder and (b) two cylinders. The simulations have been performed using a finer mesh (2560 × 256).

2. Mesh and time-step dependency

Cartoons depicting coarse numerical meshes (320 × 32) close to the cylinders in the channels having single and double cylinders have been shown in Fig. 13(a) and Fig. 13(b), respectively. The pressure drop across the channel has been used as a simple metric to perform the mesh and time-step dependence study [38]. The simulations become mesh independence even at the maximum Wi explored in the present study for $n_x \times n_y > 2000 \times 200$ [Figs. 14(a) and 14(b)]. Therefore, we have used $n_x \times n_y = 2560 \times 256$ to perform the simulations in the present study. The time step in the simulation has been controlled using the maximum Courant number ($\mathrm{Co_{max}}$) . The Courant number has been been defined as:

$$\mathrm{Co} = \frac{\Delta \mathrm{t}}{2\mathrm{V}} \sum_{\mathrm{faces_i}} |\phi_{\mathrm{i}}|, \tag{A2}$$

where Δt and V are the simulation time step and cell volume, respectively. ϕ_i is the cell-face volumetric flux and $\sum_{\mathrm{faces}_i}$ represents the summation over all the faces of a given cell. We have fixed $\mathrm{Co_{max}} = 0.025$ in the present study as the simulation result becomes time-step independent for $\mathrm{Co_{max}} < 0.035$ [Fig. 14(a)].

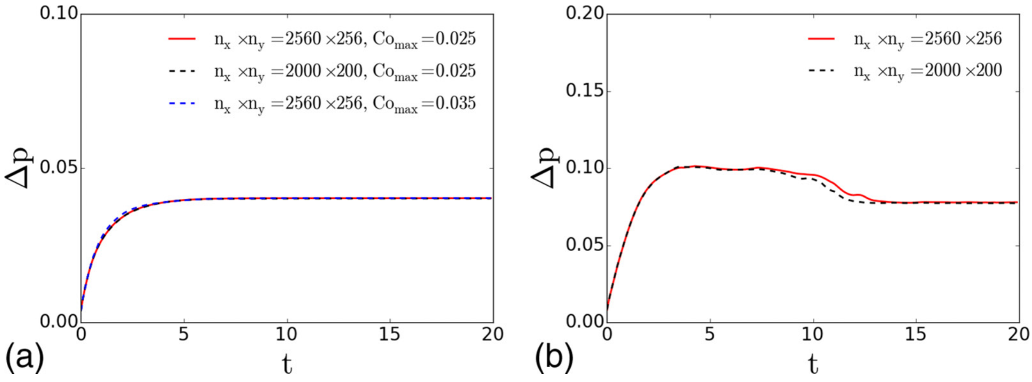

FIG. 14. Normalized pressure drop across the channel having a single cylinder at (a) Wi = 0.62 and (b) Wi = 3.12.

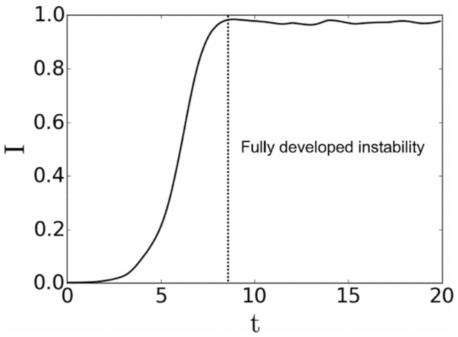

FIG. 15. Time-dependent flow asymmetry around the confined cylinder at Wi $= 3.12$. Other parameters are $\beta = 0.05$ and $L^2 = 1000$. The standard deviation of the fluctuation of I once the asymmetric flow state becomes fully developed is $\approx$0.6% of the mean value.

3. Time-dependent flow asymmetry around cylinder for a fixed flow rate

The flow through the channel after the instability for the simulation at a constant flow rate (or Wi) becomes almost steady even at the maximum Wi (Wi $= 3.12$). Figure 15 depicts the time-dependent flow asymmetry (I) around the confined cylinder at Wi $= 3.12$. Once the asymmetric flow state becomes fully developed, the value of I fluctuates around a well-defined mean with a very small standard deviation ($< 1\%$ of the mean value) (Fig. 15). Hence, the flow can be considered almost steady.

4. Quasistatic variation of flow rate

The continuous variation of the flow rate (i.e., Wi) does not allow stress to relax and hence leads to hysteresis in the present study. For a quasistatic variation of Wi [29,63], we have plotted the time-dependent flow asymmetry around the confined cylinder in Fig. 16. The stress field, or the flow asymmetry, does not respond instantaneously to the change in Wi and hence there is a time lag (Fig. 16). The lag time of the stress to respond the increment and decrement of Wi are $\Delta t_{\text{up}} = 7.7$ and $\Delta t_{\text{down}} = 12.2$, respectively (Fig. 16). Therefore, if the time step (Δt_{step}) of the quasistatic variation of Wi is $\Delta t_{\text{step}} > \max(\Delta t_{\text{up}}, \Delta t_{\text{down}})$, the stress has sufficient time to relax and the flow state does not exhibit hysteresis as shown in Fig. 16.

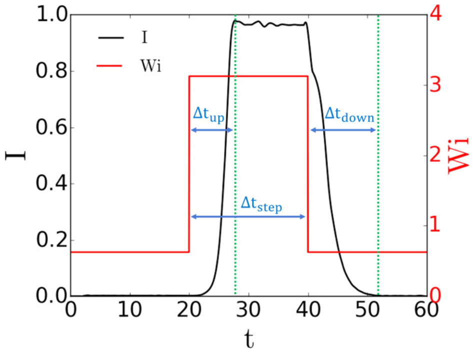

FIG. 16. Flow asymmetry around a confined cylinder for a quasistatic variation of Wi (flow rate) at $\beta = 0.05$ and $L^2 = 1000$. $\Delta t_{\text{up}} = 7.7$ and $\Delta t_{\text{down}} = 12.2$ are the lag time of the stress to respond to the increment and decrement of Wi, respectively. The time step of the quasistatic variation of Wi is $\Delta t_{\text{step}} = 20$.

[1] M. Kumar, J. S. Guasto, and A. M. Ardekani, Transport of complex and active fluids in porous media, J. Rheol. **66**, 375 (2022).

[2] L. Hall-Stoodley, J. W. Costerton, and P. Stoodley, Bacterial biofilms: from the Natural environment to infectious diseases, Nat. Rev. Microbiol. **2**, 95 (2004).

[3] K. S. Sorbie, *Polymer-Improved Oil Recovery* (Springer Science & Business Media, New York 2013).

[4] D. J. Smith, E. A. Gaffney, and J. R. Blake, Modelling mucociliary clearance, Respir. Physiol. Neurobiol. **163**, 178 (2008).

[5] P. Stoodley, I. Dodds, D. De Beer, H. L. Scott, and J. D. Boyle, Flowing biofilms as a transport mechanism for biomass through porous media under laminar and turbulent conditions in a laboratory reactor system, Biofouling **21**, 161 (2005).

[6] D. Roote, Technology status report: In situ flushing, Ground Water Remediation Technology Analysis Center (1998), http://www.gwrtac.org.

[7] S. Aramideh, P. P. Vlachos, and A. M. Ardekani, Pore-scale statistics of flow and transport through porous media, Phys. Rev. E **98**, 013104 (2018).

[8] C. A. Browne, A. Shih, and S. S. Datta, Pore-scale flow characterization of polymer solutions in microfluidic porous media, Small **16**, 1903944 (2019).

[9] D. Kawale, G. Bouwman, S. Sachdev, P. L. Zitha, M. T. Kreutzer, W. R. Rossen, and P. E. Boukany, Polymer conformation during flow in porous media, Soft Matter **13**, 8745 (2017).

[10] P. Pakdel and G. H. McKinley, Elastic Instability and Curved Streamlines, Phys. Rev. Lett. **77**, 2459 (1996).

[11] G. H. McKinley, P. Pakdel, and A. Öztekin, Rheological and geometric scaling of purely elastic flow instabilities, J. Non-Newton. Fluid Mech. **67**, 19 (1996).

[12] K. Weissenberg, A continuum theory of rhelogicalphenomena, Nature **159**, 310 (1947).

[13] P. E. Arratia, C. C. Thomas, J. Diorio, and J. P. Gollub, Elasticinstabilities of Polymer Solutions in Cross-Channel Flow, Phys. Rev. Lett. **96**, 144502 (2006).

[14] R. J. Poole, M. A. Alves, and P. J. Oliveira, Purely Elastic Flow Asymmetries, Phys. Rev. Lett. **99**, 164503 (2007).

[15] A. Groisman and V. Steinberg, Elastic turbulence in a polymer solution flow, Nature (Lond.) **405**, 53 (2000).

[16] D. M. Walkama, N. Waisbord, and J. S. Guasto, Disorder Suppresses Chaos in Viscoelastic Flows, Phys. Rev. Lett. **124**, 164501 (2020).

[17] A. Groisman and V. Steinberg, Efficient mixing at low reynolds numbers using polymer additives, Nature (Lond.) **410**, 905 (2001).

[18] C. A. Browne and S. S. Datta, Elastic turbulence generates anomalous flowresistance in porous media, Sci. Adv. **7**, 1 (2021).

[19] S. J. Haward, G. H. Mckinley, and A. Q. Shen, Elastic instabilities in planar elongational flow of monodisperse polymer solutions, Sci. Rep. **6**, 33029 (2016).

[20] L. E. Rodd, T. P. Scott, D. V. Boger, J. J. Cooper-White, and G. H. McKinley, The inertio-elastic planar entry flow of low-viscosity elastic fluids in micro-fabricated geometries, J. Non-Newton. Fluid Mech. **129**, 1 (2005).

[21] A. Lanzaro and X.-F. Yuan, Effects of contraction ratio on non-linear dynamics of semi-dilute, highly polydisperse paam solutions in microfluidics, J. Non-Newton. Fluid Mech. **166**, 1064 (2011).

[22] G. Batchelor, The stress generated in a non-dilute suspension of elongated particles by pure straining motion, J. Fluid Mech. **46**, 813 (1971).

[23] D. V. Boger, Viscoelastic flows through contractions, Annu. Rev. Fluid Mech. **19**, 157 (1987).

[24] A. Mongruel and M. Cloitre, Extensional flow of semidilute suspensions of rod-like particles through an orifice, Phys. Fluids **7**, 2546 (1995).

[25] A. Mongruel and M. Cloitre, Axisymmetric orifice flow for measuring the elongational viscosity of semi-rigid polymer solutions, J. Non-Newton. Fluid Mech. **110**, 27 (2003).

[26] S. Kenney, K. Poper, G. Chapagain, and G. F. Christopher, Large deborah number flows around confined microfluidic cylinders, Rheol. Acta **52**, 485 (2013).

[27] X. Shi, S. Kenney, G. Chapagain, and G. F. Christopher, Mechanisms of onset for moderate mach number instabilities of viscoelastic flows around confined cylinders, Rheol. Acta **54**, 805 (2015).

[28] B. Qin, P. F. Salipante, S. D. Hudson, and P. E. Arratia, Upstream vortex and elastic wave in the viscoelastic flow around a confined cylinder, J. Fluid Mech. **864**, R2 (2019).

[29] S. J. Haward, C. C. Hopkins, and A. Q. Shen, Asymmetric flow of polymer solutions around microfluidic cylinders: Interaction between shear-thinning and viscoelasticity, J. Non-Newton. Fluid Mech. **278**, 104250 (2020).

[30] S. Varchanis, C. C. Hopkins, A. Q. Shen, J. Tsamopoulos, and S. J. Haward, Asymmetric flows of complex fluids past confined cylinders: A comprehensive numerical study with experimental validation, Phys. Fluids **32**, 053103 (2020).

[31] J. A. Deiber and W. R. Schowalter, Modeling the flow of viscoelastic fluids through porous media, AIChE J. **27**, 912 (1981).

[32] M. J. Blunt, *Multiphase Flow in Permeable Media: A Pore-scale Perspective* (Cambridge University Press, Cambridge, London, 2017).

[33] X. Shi and G. F. Christopher, Growth of viscoelastic instabilities around linear cylinder arrays, Phys. Fluids **28**, 124102 (2016).

[34] C. A. Browne, A. Shih, and S. S. Datta, Bistability in the unstable flow of polymer solutions through pore constriction arrays, J. Fluid Mech. **890**, A2 (2020).

[35] A. Varshney and V. Steinberg, Elastic wake instabilities in a creeping flow between two obstacles, Phys. Rev. Fluids **2**, 051301(R) (2017).

[36] M. Kumar and A. M. Ardekani, Elastic instabilities between two cylinders confined in a channel, Phys. Fluids **33**, 074107 (2021).

[37] M. Kumar and A. M. Ardekani, Viscoelastic instability in an asymmetric geometry, Eur. Phys. J. Spec. Top. (2022), doi: 10.1140/epjs/s11734-022-00657-9.

[38] M. Kumar, S. Aramideh, C. A. Browne, S. S. Datta, and A. M. Ardekani, Numerical investigation of multistability in the unstable flow of a polymer solution through porous media, Phys. Rev. Fluids **6**, 033304 (2021).

[39] D. Kawale, E. Marques, P. L. Zitha, M. T. Kreutzer, W. R. Rossen, and P. E. Boukany, Elastic instabilities during the flow of hydrolyzed polyacrylamide solution in porous media: Effect of pore-shape and salt, Soft Matter **13**, 765 (2017).

[40] S. J. Haward, C. C. Hopkins, and A. Q. Shen, Stagnation points control chaotic fluctuations in viscoelastic porous media flow, Proc. Natl. Acad. Sci. USA **118**, e2111651118 (2021).

[41] M. Kumar, J. S. Guasto, and A. M. Ardekani, Lagrangian stretching reveals stress topology in viscoelastic flows, arXiv:2206.11800.

[42] C. Gin and P. Daripa, Time-dependent injection strategies for multilayer Hele-Shaw and porous media flows, Phys. Rev. Fluids **6**, 033901 (2021).

[43] Q. Yuan and J. Azaiez, Miscible displacements in porous media with time-dependent injection velocities, Transp. Porous Media **104**, 57 (2014).

[44] C. Pankiewitz and E. Meiburg, Miscible porous media displacements in the quarter five-spot configuration. Part 3. Non-monotonic viscosity profiles, J. Fluid Mech. **388**, 171 (1999).

[45] S. Aramideh, P. P. Vlachos, and A. M. Ardekani, Unstable displacement of non-aqueous phase liquids with surfactant and polymer, Transp. Porous Media **126**, 455 (2019).

[46] A. B. Mann, S. Shaheen, K. Maqbool, and S. Poncet, Fractional Burgers fluid flow due to metachronal ciliary motion in an inclined tube, Front. Physiol. **10**, 588 (2019).

[47] B. K. Huang and M. A. Choma, Microscale imaging of cilia-driven fluid flow, Cell. Molec. Life Sci. **72**, 1095 (2015).

[48] R. Bird, R. Armstrong, and O. Hassager, *Dynamics of Polymeric Liquids: Fluid Mechanics*, 2nd ed. (John Wiley & Sons Inc., New York, 1987), Vol. 1.

[49] R. B. Bird, C. F. Curtiss, R. C. Armstrong, and O. Hassager, *Dynamics of Polymeric Liquids: Kinetic Theory*, 2nd ed. (Wiley, New York, 1987), Vol. 2.

[50] R. B. Bird, P. J. Dotson, and N. L. Johnson, Polymer solution rheology based on a finitely extensible bead-spring chain model, J. Non-Newton. Fluid Mech. **7**, 213 (1980).

[51] M. D. Chilcott and J. M. Rallison, Creeping flow of dilute polymer solutions past cylinders and spheres, J. Non-Newton. Fluid Mech. **29**, 381 (1988).

[52] P. J. Oliveira, An exact solution for tube and slit flow of a FENE-P fluid, Acta Mech. **158**, 157 (2002).

[53] J. G. Oldroyd, On the formulation of rheological equations of state, Proc. Roy. Soc. Lond. Ser. A, Math. Phys. Sci. **200**, 523 (1950).

[54] D. Boger, A highly elastic constant-viscosity fluid, J. Non-Newton. Fluid Mech. **3**, 87 (1977).

[55] K. Walters and M. F. Webster, The distinctive CFD challenges of computational rheology, Int. J. Numer. Methods Fluids **43**, 577 (2003).

[56] R. Fattal and R. Kupferman, Constitutive laws for the matrix-logarithm of the conformation tensor, J. Non-Newton. Fluid Mech. **123**, 281 (2004).

[57] R. Fattal and R. Kupferman, Time-dependent simulation of viscoelastic flows at high Weissenberg number using the log-conformation representation, J. Non-Newton. Fluid Mech. **126**, 23 (2005).

[58] H. Jasak, A. Jemcov, and Z. Tukovic, Openfoam: A c + + library for complexphysics simulations, in *Proceedings of the International Workshop on Coupled Methods in Numerical Dynamics* (IUC, Dubrovnik Croatia, 2007).

[59] F. Pimenta and M. A. Alves, Stabilization of an open-source finite-volume solver for viscoelastic fluid flows, J. Non-Newton. Fluid Mech. **239**, 85 (2017).

[60] F. Habla, M. W. Tan, J. Haßlberger, and O. Hinrichsen, Numerical simulation of the viscoelastic flow in a three-dimensional lid-driven cavity using the log-conformation reformulation in OpenFOAM®, J. Non-Newton. Fluid Mech. **212**, 47 (2014).

[61] J. M. Dealy, Weissenberg and deborah numbers-their definition and use, Rheol. Bull. **79**, 14 (2010).

[62] G. H. McKinley, R. C. Armstrong, and R. A. Brown, The wake instability in viscoelastic flow past confined circular cylinders, Philos. Trans. Roy. Soc. Lond. Ser. A: Phys. Eng. Sci. **344**, 265 (1993).

[63] S. J. Haward, N. Kitajima, K. Toda-Peters, T. Takahashi, and A. Q. Shen, Flow of wormlike micellar solutions around microfluidic cylinders with high aspect ratio and low blockage ratio, Soft Matter **15**, 1927 (2019).

[64] T. L. Bergman, F. P. Incropera, D. P. DeWitt, and A. S. Lavine, *Fundamentals of Heat and Mass Transfer* (John Wiley & Sons, New York, 2011).